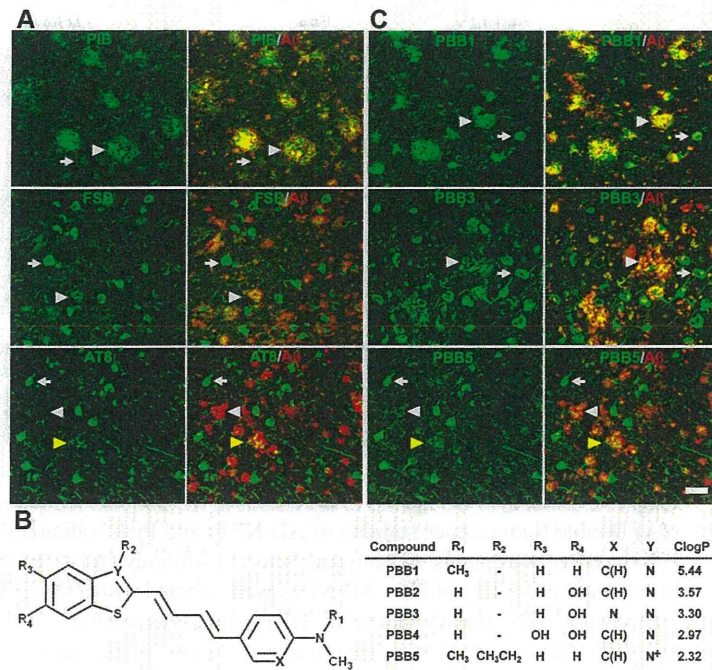## Highlights

1. Compounds for *in vivo* imaging of diverse types of tau inclusions were developed.

2. These compounds enabled optical and PET imaging of tau lesions in model mice.

3. PET with one of these compounds illuminated tau-rich regions in Alzheimer's disease.

4. Our probe produced PET images consistent with spreading tau pathology.

| Compound | R₁ | R₂ | R₃ | R₄ | X | Y | ClogP |

| Compound	R_1	R_2	R_3	R_4	X	Y	ClogP
PBB1	CH_3	-	H	H	C(H)	N	5.44
PBB2	H	-	H	OH	C(H)	N	3.57
PBB3	H	-	H	OH	N	N	3.30
PBB4	H	-	OH	OH	C(H)	N	2.97
PBB5	CH_3	CH_3CH_2	H	H	C(H)	N^+	2.32

**Figure 1. Design and characterization of PBB compounds as potential imaging agents for tauopathies**

(A) Confocal fluorescence images of frontal cortex sections from an AD patient. Following fluorescence labeling (pseudocolors are converted to green) with PIB (top row) and FSB (middle row), the samples were immunostained with an antibody against A βN3(pE) (red in the right column). PIB intensely labeled A βplaques (white arrowheads), but did not clearly label NFTs (arrows). By contrast, NFTs and neuropil threads were intensely labeled by FSB, while the staining of diffuse plaques was negligible. A section was also doubly immunolabeled (bottom row) with AT8 (green) and anti-A βN3(pE) antibodies (red in the right panel), to demonstrate the abundance of tau and A βamyloids in this area. Yellow arrowheads indicate tau-positive dystrophic neurites associated with senile plaques. (B) Structures of PBBs. Neutral benzothiazoles (PBB1–4) are newly synthesized chemicals, and a charged benzothiazolium, PBB5, is identical to a commercially available near-infrared laser dye. (C) Confocal fluorescence images of PBBs (pseudocolors are converted to green) and A βN3(pE) (red in the right column) staining in sections adjacent to those displayed in A. The intensity of plaque staining (arrowheads) relative to that of NFTs (arrows) was positively associated with the lipophilicity of PBBs. As compared with PBB1 (top row) staining, labeling of diffuse plaques with PBB3 (middle row) was substantially attenuated. PBB5 was nearly unreactive with diffuse plaques (bottom row), and subsequent double immunofluorescence staining of the same section (bottom row in C) illustrated good agreement of PBB5 labeling with the distribution of AT8-positive NFTs. Scale bar: 50 μm (A, C).
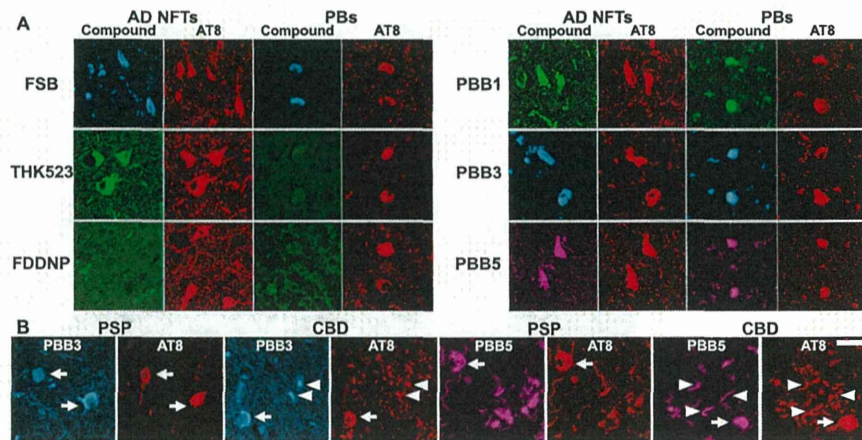
Figure 2. Binding of tau ligands to tau lesions in AD and non-AD tauopathy brains
(A) Double fluorescence staining of AD NFTs and Pick bodies (PBs) in Pick's disease with
PBBs, other tau ligands and anti-phospho-tau antibody (AT8). FSB and PBBs sensitively
captured AD NFTs and PBs. AD NFTs were labeled with THK523. Meanwhile, PBs were
not visualized by these compounds. NFTs and PBs were barely recognizable by using
FDDNP. (B) Double fluorescence staining of neuronal tau inclusions (arrows) in PSP and
CBD and putative astrocytic plaques (arrowheads) in CBD. A substantial portion of tau
fibrils in neurons were captured by PBB3 and PBB5, but a much smaller subset of
phosphorylated tau aggregates in astrocytic plaques were labeled with these compounds.
Scale bar: 20 μm (A, B).
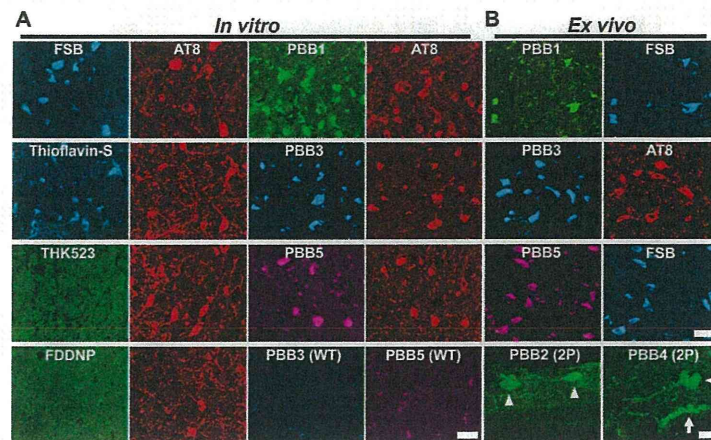
Figure 3. *In vitro* **and** *ex vivo* **labeling of NFTs in PS19 mice with PBB compounds**
(**A**) Double fluorescence staining of intraneuronal tau aggregates in postmortem brain stem slices of a 12-month-old PS19 mouse with PBB, other amyloid ligands and anti-phospho-tau antibody (AT8). (**B**) Binding of intravenously administered PBBs (0.1 mg/kg PBB5 and 1 mg/kg PBB1 and PBB3) to NFTs in PS19 mice at 10–12 months of age. The tissues were sampled at 60 min after tracer administration. The brain stem (top row) and spinal cord (second and third rows from the top) sections abundantly contained neurons showing strong fluorescence (left), and subsequent staining with FSB or AT8 (right) indicated that these cells were laden with tau amyloid fibrils (right). Putative intraneuronal tau inclusions in unsectioned spinal cords (arrowheads in the bottom row) removed from PS19 mice at 60 min after intravenous injection of PBB2 and PBB4 were also clearly visible by using a two-photon (2P) fluorescence microscopic system. Arrow in the bottom row indicates a cluster of autofluorescence signals from blood cells. Scale bars: 25 μm (**A**); 30 μm (top to third rows in **B**); 20 μm (bottom row in **B**).
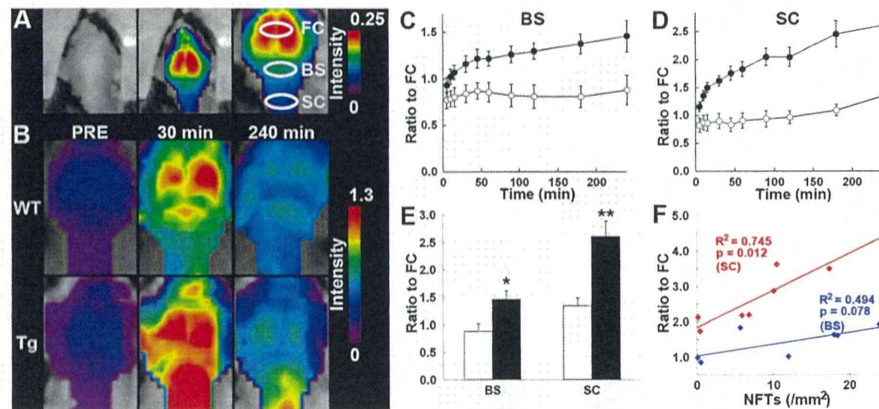
Figure 4. Noninvasive near-infrared imaging of tau pathology in living tau Tg mice using pulsed laser optics and PBB5

(A) Baseline autofluorescence signals (middle) are overlaid on the visible background image of a shaven non-Tg WT mouse head (left). Ellipsoidal ROIs are defined above the frontal cortex (FC), brain stem (BS) and cervical spinal cord (SC) guided by a relatively intense emission from the FC region (right). **(B)** Fluorescence intensity maps in 12-month-old WT (top) and PS19 (Tg; bottom) mice before and at 30 and 240 min after the intravenous administration of PBB5 (0.1 mg/kg). The intensity maps **(A, B)** are normalized by the FC ROI value at 30 min after tracer injection. Long-lasting retention of the tracer was noted in the BS and SC ROIs of the Tg mouse. **C, D,** Target-to-FC ratios of fluorescence intensity in the BS **(C)** and SC **(D)** ROIs over the image acquisition time in the WT (open circles; n = 7) and PS19 (closed circles; n = 7) mice. There were significant main effects of time, region and genotype in 2-way, repeated-measures ANOVA (time, $F_{(11, 132)} = 17.6$, $p < 0.001$; region, $F_{(1, 12)} = 29.9$, $p < 0.001$; genotype, $F_{(1, 12)} = 23.6$, $p < 0.001$). **(E)** Target-to-FC ratios in the BS and SC ROIs of the WT (open columns) and tau Tg (closed columns) mice at 240 min after tracer injection. *, $p < 0.05$; **, $p < 0.01$; 2-way repeated-measures ANOVA with Bonferroni's post hoc analysis. **(F)** Scatterplots of target-to-FC ratios at 240 min versus the number of FSB-positive NFTsper unit area of postmortem 20 - μm tissue slices in BS (blue symbols) and SC (red symbols) ROIs of tau Tg mice. Solid lines represent regressions; p values were determined by t-test. Vertical bars in the graphs represent SEs.
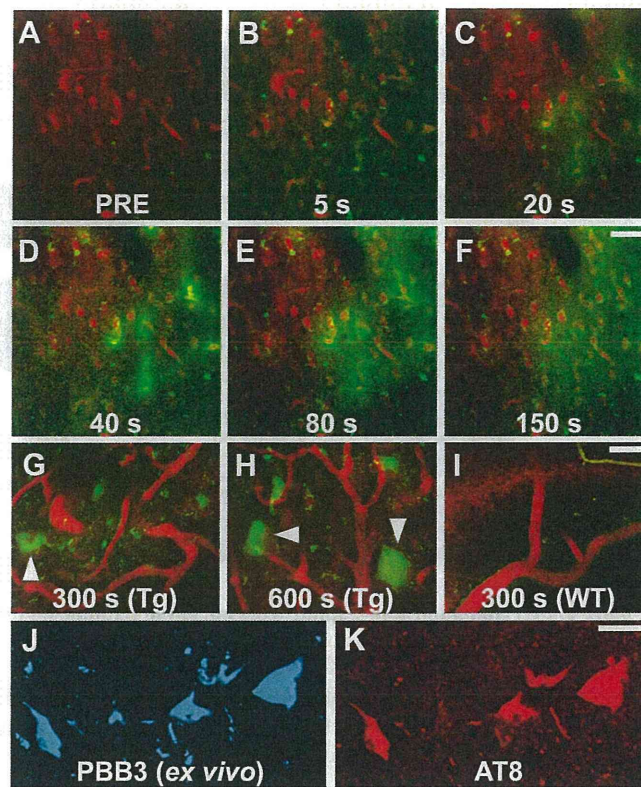
Figure 5. Real-time two-photon laser scanning images of PBB3 diffusing from vessels, binding to intraneuronal tau inclusions, and clearing from spinal cord
(A–H) A maximum projection of fluorescence in a 3-D volume of the spinal cord of a living PS19 mouse at 12 months of age before (A) and at various time points after (B–H) intravenous administration of PBB3 (1 mg/kg). Blood vessels were labeled with Sulforhodamine 101 (red) intraperitoneally injected at 15 min before PBB3 administration. Green fluorescence indicates a rapid transfer of PBB3 from the plasma to tissue parenchyma (B–E) and subsequent washout from the tissue (F). Background PBB3 signals were further attenuated beyond 300 sec, while somatodendritic labeling by this compound was observed in a subset of neurons (arrowheads in G, H). (I) Fluorescence image of WT spinal cord at 300 sec after PBB3 injection, demonstrating no overt retention of the tracer in the tissue. (J, K) *Ex vivo* microscopy for a brain stem section of the same Tg mouse. Tissues were obtained at 60 min after PBB3 injection. Signals of intravenously administered PBB3 (J) overlapped with AT8 immunoreactivity (K). Scale bars: 50 μm (A–F); 25 μm (G–I), 25 μm (J, K).
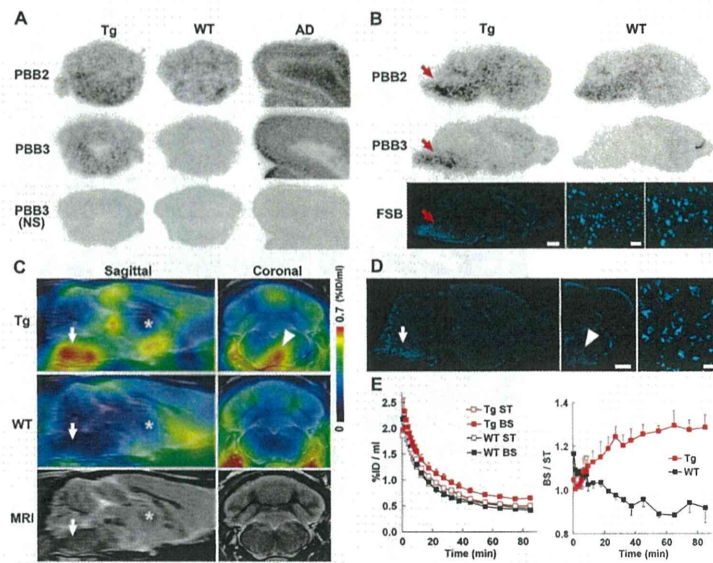
**Figure 6. PET and autoradiographic detection of tau pathologies in PS19 mice using [^{11}C]PBB2 and [^{11}C]PBB3**

(A) *In vitro* autoradiograms of PS19 and non-Tg WT hindbrains (coronal sections) and AD frontal cortex. Fibrillar aggregates in the mouse brain stem and AD gray matter produced intense radiolabeling with both tracers, but nonspecific background signals were also observed at a considerably high level with the use of [^{11}C]PBB2. Binding of [^{11}C]PBB3 was profoundly abolished by the addition of nonradioactive PBB3 (10 μM). (B) Autoradiographic labeling with intravenously injected [^{11}C]PBB2 and [^{11}C]PBB3 in PS19 (Tg) and WT mice. The brains were removed at 45 min after injection, and were cut into sagittal slices. The autoradiographic section of PS19 brain was also stained with FSB. Arrows indicate the brain stem containing numerous tau inclusions displayed at intermediate and high magnifications. (C) Sagittal and coronal PET images generated by averaging dynamic scan data at 60–90 min after intravenous administration of [^{11}C]PBB3. The images are overlaid on the MRI template (images of the template alone are presented at the bottom). Arrows and asterisks indicate the brain stem and striatum, respectively, and arrowhead denotes intense radiolabeling in the medial brain stem of the PS19 mouse. (D) FSB staining of PS19 mouse brain shown in c. Sagittal (left) and coronal (middle) images and a high-power view of fibrillar inclusions (right) are displayed. Corresponding to high-level retention of [^{11}C]PBB3 in PET scans, abundant FSB-positive lesions were found in the medial brain stem (arrow and arrowhead). (E) Time-radioactivity curves (left) in the striatum (ST) and brain stem (BS) and BS-to-ST ratio of radioactivity (right) over the imaging time in PS19 (Tg; red symbols) and WT (black symbols) mice (n = 5 each). Vertical bars in the graphs denote SEs. Scale bars: 1 cm (A, top, middle and bottom-left panels in B); 1 cm (C, left and middle panels in D); 100 μm (bottom-middle panel in B); 100 μm (bottom-right panel in B, right panel in D).
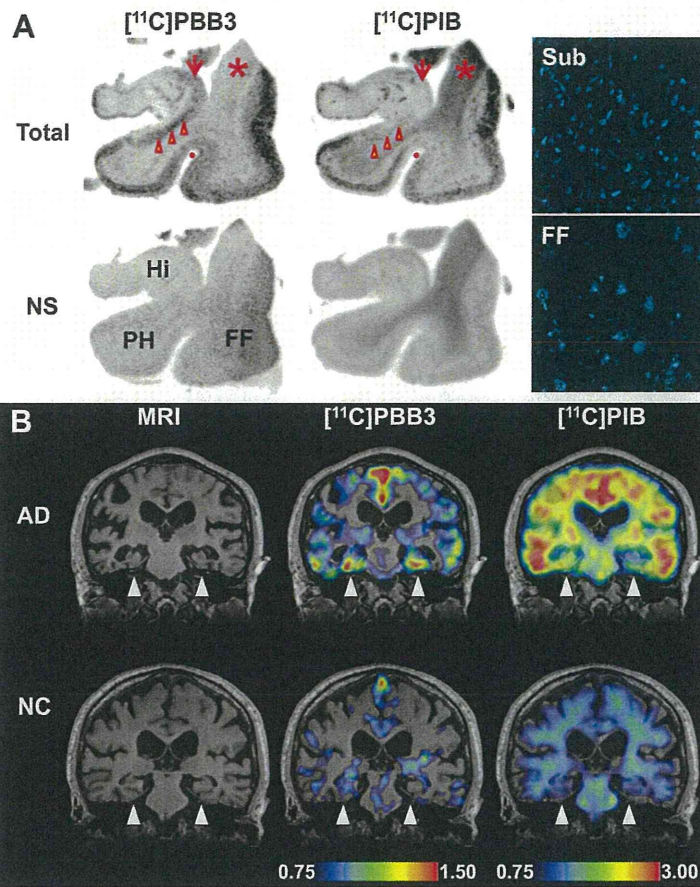
Figure 7. Accumulation of [11C]PBB3 in the hippocampal formation of AD patients revealed by *in vitro* autoradiography and *in vivo* PET

(A) Autoradiographic labeling of adjacent brain sections from an AD patient with 10 nM of [11C]PBB3 (left) and [11C]PIB (middle). The slices contain the hippocampus (Hi), parahippocampal gyrus (PH), fusiform gyrus (FF) and white matter (asterisks). Total binding (top) of [11C]PBB3 and [11C]PIB was markedly abolished (bottom) by addition of nonradioactive PBB5 (100 μM) and thioflavin-S (10 μM), respectively, except for the nonspecific (NS) labeling of white matter with [11C]PIB. The hippocampal CA1 sector and subiculum displayed intense [11C]PBB3 signals without noticeable binding of [11C]PIB, and binding of [11C]PBB3 in cortical areas flanking the collateral sulcus (identified by a red dot) and hippocampal CA2 sector (arrows) was also abundant relative to that of [11C]PIB. FSB staining of amyloid fibrils in the sections used for autoradiography indicated the predominance of NFTs and diffuse plaques in the hippocampal subiculum (Sub) and fusiform gyrus (FF), respectively (right panels), supporting the strong reactivity of [11C]PBB3 with AD NFTs. (B) MRI (left) and PET imaging with [11C]PBB3 (middle) and [11C]PIB (right) performed in the same AD (top) and normal control (NC; bottom) subjects. Coronal images containing the hippocampal formation (arrowheads) are displayed. [11C]PBB3- and [11C]PIB-PET images were generated by estimating SUVRs at 30–70 min and 50–70 min after radiotracer injection, respectively, and were superimposed on individual MRI data. In the hippocampal formation, prominently increased retention of [11C]PBB3 in the AD patient was in sharp contrast to the modest or negligible changes in

[^{11}C]PIB binding as compared with NC. Scale ranges for SUVRs were 0.75–1.50 ([^{11}C]PBB3) and 0.75–3.00 ([^{11}C]PIB).
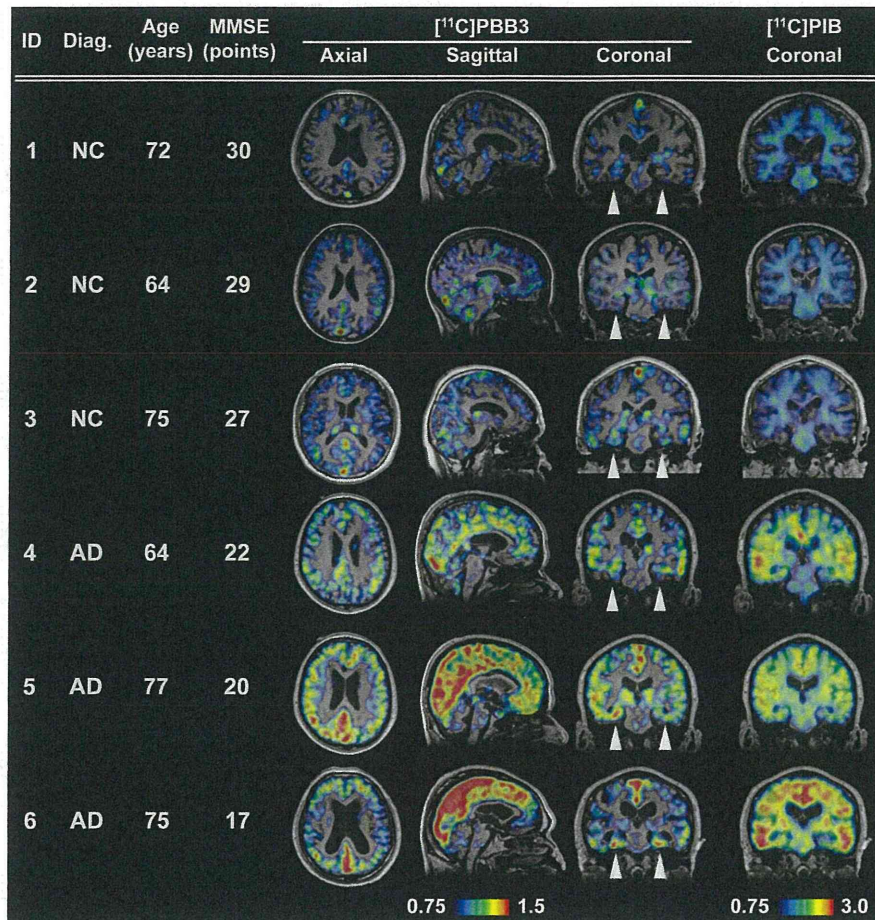
Figure 8. Orthogonal [11C]PBB3-PET images in all human subjects examined in the present exploratory clinical study

Data are displayed as parametric maps for SUVR. The [11C]PBB3 binding to the hippocampal formation (arrowheads) was increased consistently in AD patients in contrast to minimum radiotracer retention in normal control (NC) subjects with MMSE score of 29–30 points (Subjects 1 and 2). Another NC subject with MMSE score of 27 points (Subject 3) was negative for [11C]PIB-PET, but exhibited slight accumulation of radiotracer signals primarily around the hippocampus, resembling fibrillar tau deposition at Braak stage III–IV or earlier. Sagittal slices around the midline illustrate that radioligand signals were the most intense in the limbic system but began to expand to the neocortex in a patient with the mildest AD (Subject 4), in agreement with the tau pathology at Braak stage V–VI, and was further intensified in most neocortical areas, corresponding to Braak stage VI, apparently as a function of the disease severity assessed by MMSE (Subjects 5 and 6). The AD patient with the lowest MMSE score (Subject 6) displayed less profound increase of [11C]PBB3 retention in the lateral temporal and parietal cortices than did the other two AD cases, and this is attributable to marked cortical atrophy in this individual and/or toxic loss of tau-bearing neurons in these brain areas at an advanced pathological stage. In contrast to the spatial profiles of [11C]PBB3 binding, the distribution of [11C]PIB signals appeared unchanged among AD subjects.
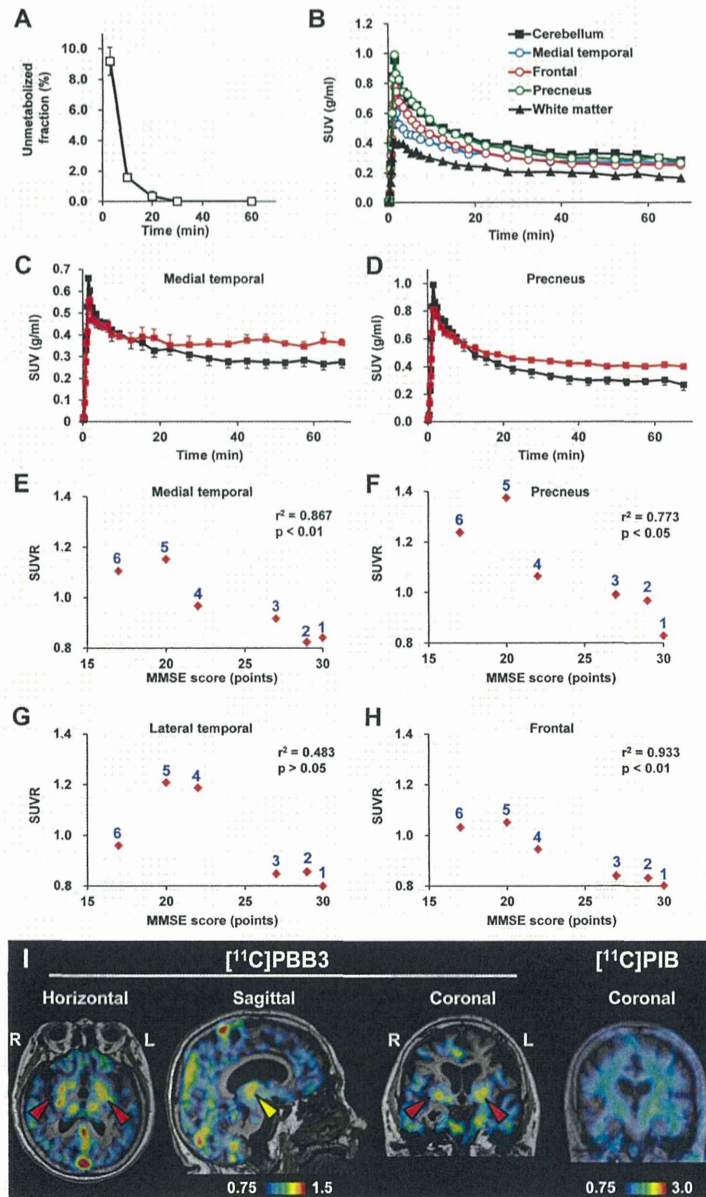
Figure 9. Pharmacokinetic profiles of [^{11}C]PBB3 administered to humans and PET images of a patient clinically diagnosed as having corticobasal syndrome

(A) Time course of unmetabolized [^{11}C]PBB3 fraction in plasma following intravenous radiotracer injection. The plot was generated by averaging data from 6 individuals. (B) Time-radioactivity curves in different brain regions of cognitively normal control subjects over 70 min after intravenous injection of [^{11}C]PBB3. Data were generated by averaging values in two individuals, and are presented as standard uptake values (SUVs). (C, D) Comparisons of time-radioactivity curves in the medial temporal region (C) and precuneus (D) of normal controls (black symbols and lines; n = 3) and AD patients (red symbols and lines; n = 3). (E–H) Scatterplots illustrating correlation of SUVRs with MMSE scores in the medial temporal region (E), precuneus (F) and lateral temporal (G) and frontal (H) cortices.

Numbers beside symbols denote subject ID as indicated in Fig. 8. Coefficients of determination (r^2) and p values by t-test are displayed in graphs. **(I)** [^{11}C]PBB3- and [^{11}C]PIB-PET images in a subject with clinical diagnosis of corticobasal syndrome. Images were generated as in Figs. 7 and 8. Accumulation of [^{11}C]PBB3 was noticeable in the basal ganglia (red arrowheads) with right-side dominance and an area containing the thalamus and midbrain (yellow arrowhead).

EJNMMI Research
a SpringerOpen Journal

ORIGINAL RESEARCH   **Open Access**

Evaluation of the biodistribution and radiation dosimetry of the ^{18}F-labelled amyloid imaging probe [^{18}F]FACT in humans

Miho Shidahara[1,2*], Manabu Tashiro[2], Nobuyuki Okamura[3], Shozo Furumoto[3], Katsutoshi Furukawa[4], Shoichi Watanuki[2], Kotaro Hiraoka[2], Masayasu Miyake[2], Ren Iwata[5], Hajime Tamura[1], Hiroyuki Arai[4], Yukitsuka Kudo[6] and Kazuhiko Yanai[2,3]

Abstract

Background: The biodistribution and radiation dosimetry of the ^{18}F-labelled amyloid imaging probe ([^{18}F] FACT) was investigated in humans.

Methods: Six healthy subjects (three males and three females) were enrolled in this study. An average of 160.8 MBq of [^{18}F] FACT was intravenously administered, and then a series of whole-body PET scans were performed. Nineteen male and 20 female source organs, and the remainder of the body, were studied to estimate time-integrated activity coefficients. The mean absorbed dose in each target organ and the effective dose were estimated from the time-integrated activity coefficients in the source organs. Biodistribution data from [^{18}F] FACT in mice were also used to estimate absorbed doses and the effective dose in human subjects; this was compared with doses of [^{18}F] FACT estimated from human PET data.

Results: The highest mean absorbed doses estimated using human PET data were observed in the gallbladder (333 ± 251 µGy/MBq), liver (77.5 ± 14.5 µGy/MBq), small intestine (33.6 ± 30.7 µGy/MBq), upper large intestine (29.8 ± 15.0 µGy/MBq) and lower large intestine (25.2 ± 12.6 µGy/MBq). The average effective dose estimated from human PET data was 18.6 ± 3.74 µSv/MBq. The highest mean absorbed dose value estimated from the mouse data was observed in the small intestine (38.5 µGy/MBq), liver (25.5 µGy/MBq) and urinary bladder wall (43.1 µGy/MBq). The effective dose estimated from the mouse data was 14.8 µSv/MBq for [^{18}F] FACT.

Conclusions: The estimated effective dose from the human PET data indicated that the [^{18}F] FACT PET study was acceptable for clinical purposes.

Keywords: Positron emission tomography, Radiation dosimetry, Amyloid imaging, MIRD, [^{18}F] FACT

Background

Amyloid beta imaging

Deposits of amyloid β (Aβ) plaque are one of the pathological observations in patients with Alzheimer's disease (AD); Aβ deposition progresses at an earlier point than the current clinical diagnostic point for this disease [1]. For earlier diagnosis of AD and the evaluation of treatment efficacy, *in vivo* amyloid imaging using positron emission tomography (PET), which provides quantitation and visualisation of Aβ deposition in the brain, is useful. Therefore, several Aβ-binding probes dedicated for PET imaging have been developed [2,3].

Most of these PET Aβ ligands are ^{11}C-labelled compounds (physical half life ($T_{1/2}$), 20 min), and ^{18}F-labelled agents are being increasingly investigated owing to their long half life ($T_{1/2}$, 109.7 min). The long $T_{1/2}$ of ^{18}F enables several PET scans to be carried out from a single synthesis of labelled agent and also enables its commercial distribution to any PET facility. On the other hand, the longer the $T_{1/2}$ of the radioisotope gets, the greater is the radiation

* Correspondence: shidahara@med.tohoku.ac.jp
[1]Division of Medical Physics, Tohoku University School of Medicine, 2-1 Seiryo-machi, Aoba-ku, Sendai 980-8575, Japan
[2]Division of Cyclotron Nuclear Medicine, Cyclotron Radioisotope Center, Tohoku University, Sendai 980-8578, Japan
Full list of author information is available at the end of the article

dose exposure for the PET subject for the same administered dose of radioligand.

Importance of radiation dosimetry

For subjects undergoing PET, internal radiation exposure is inevitable, and the radiation dose delivered is proportional to the level of radioactivity of the injected radioligand and the number of injections. In the case of amyloid imaging, subjects often have multiple PET scans for diagnostic or therapeutic longitudinal monitoring of Aβ aggregation in the brain. Therefore, estimation of the radiation dose exposure from each PET radioligand and the use of well-balanced PET scan protocols taking into consideration subject risk and benefit are important.

Estimation of the internal radiation dose requires a time series measurement of the biodistribution of the injected radioligand. There are two ways to establish the biodistribution of a radioligand in humans: one is to extrapolate from data obtained in animal experiments [4] and the other is to use data from a clinical whole-body PET study [5]. Data extrapolated from animal experiments have been used to estimate clinical radiation dose. However, Sakata et al. reported that in some radioligands, there were considerable differences in organ dose or kinetics between human and animal experiments and that a whole-body PET study would be desirable for the initial clinical evaluation of new PET radioligands [6].

Previous biodistribution and dosimetry study for PET amyloid imaging

Recently, radiation dose exposures from several PET amyloid imaging agents have been reported using clinical whole-body PET scans. One of the popular amyloid ligands, Pittsburgh compound B ([11C]PIB), has been extensively investigated with regard to its kinetics in the human body, and its effective radiation dose was found to be 4.74 μSv/MBq on average [7]. For 18F-labelled PET amyloid radioligands, effective doses in humans have been reported as follows: 18F-AV-45, 13 and 19.3 μSv/MBq [8,9]; 18F-GE067, 33.8 μSv/MBq [10]; and 18F-BAY94-9172, 14.7 μSv/MBq [11].

Aim of the present study

Fluorinated amyloid imaging compound ([18F]FACT) is an 18F-labelled amyloid imaging agent developed at Tohoku University [12]. Kudo and colleagues at this university have previously developed a 11C amyloid imaging agent named [11C]BF-227 [3]. [18F]FACT is derived from [11C]BF-227 by reducing its lipophilicity in order to reduce the nonspecific binding in the brain; AD patients showed significantly higher uptake of [18F]FACT in the neocortex region relative to controls [12]. However, the biodistribution of [18F]FACT in humans has not yet been investigated.

In the present study, the radiation dosimetry and biodistribution of [18F]FACT was investigated in healthy elderly subjects who are the target group for PET amyloid imaging. In order to determine the discrepancy in the estimated radiation dose between human and animal experiments, biodistribution studies in mice involving [18F]FACT were also conducted.

Methods
Subjects

PET studies were performed in three healthy male and in three healthy female volunteers (mean age ± standard deviation (SD), 76.3 ± 3.2 years). Subject characteristics are shown in Table 1. Both height and weight varied over a wide range (146 to 175 cm and 39 to 74 kg, respectively). All subjects were Japanese and were free of somatic and neuropsychiatric illness, as determined by clinical history and physical examination; one male subject (no. 1) had undergone a previous surgical operation involving gallbladder removal.

This study was approved by the Ethics Committee on Clinical Investigations of Tohoku University School of Medicine and was performed in accordance with the Declaration of Helsinki. Written informed consent was obtained from all subjects after a complete description of the study had been made.

Radiochemistry and radioligand purity

Figure 1 shows the chemical structure of 18F-FACT. The radiochemical purity of the radioligand in the present clinical study ranged from 97.8% to 98.7% (mean ± SD, 98.33 ± 0.42%). The specific radioactivity ranged from 30.6 to 347.7 GBq/μmol at the time of injection (mean ± SD, 139.9 ± 116.2 GBq/μmol).

PET study

All whole-body PET studies were performed using a SET-2400W scanner (Shimadzu Inc., Kyoto, Japan) in two-dimensional (2D) mode [13]. The PET scanner acquired 63 image slices at a centre-to-centre interval of 3.125 mm and had a spatial resolution of 3.9 mm full width at half maximum (FWHM) and a Z-axis resolution of 6.5 mm FWHM at centre field of view [13].

An overview of scan protocols is shown in Figure 2. Four emission scans and two transmission scans (before administration and intermediate emission scans) using a 68Ge/68Ga source were performed, with the exception of subject no. 1 who had three emission scans. In the present series of PET studies and in other research projects, a 15-min PET brain scan using three-dimensional (3D) mode was performed after the first emission scan. At 2 min after intravenous administration of 142 to 180 MBq [18F]FACT (mean ± SD, 160.8 ± 14.8 MBq; injection mass, 0.77 ± 0.66 ng), a series of whole-body PET

Table 1 Information regarding the human subjects

	Sex	Age (years)	Height (m)	Weight (kg)	BMI (kg/m^2)	History
Subject number						
1	M	77	1.59	61.2	24.2	Surgical removal of gallbladder
2	M	78	1.62	65	24.8	-
3	M	77	1.75	74	24.2	-
4	F	70	1.46	39	18.3	-
5	F	77	1.56	60.2	26.1	-
6	F	79	1.55	56	23.3	-
Mean ± 1 SD		76.3 ± 3.2	1.58 ± 0.75	59.2 ± 11.6	23.5 ± 2.7	

scans were performed. The schedule for the first and second transmission scans and the first, second, third and fourth emission scans was as follows: 6 positions × 4 min (24 min), 6 positions × 4 min (24 min), 6 positions × 3 min (18 min), 6 positions × 3 min (18 min), 6 positions × 3 min (18 min), and 6 positions × 4 min (24 min), respectively. The starting time of the second emission scan was different for each subject and was on average 55 min after the start of injection with a 5-min SD. The time gap between bed positions was 5 s. All emission data were reconstructed using OS-EM with iteration 16 and subset 2 after attenuation correction. Scatter correction was not performed because of the use of 2D mode data acquisition. The cross calibration factor of the scanner (Bq per ml/cps per voxel) was determined once per week using a cylindrical water phantom (25-cm length and 20-cm inner diameter) filled with ^{18}F solutions and by measuring the sample activity of the ^{18}F solutions at the well counter (BSS-3: Shimadzu Co., Ltd., Kyoto, Japan) [14].

Urination was controlled before, after and during the series of PET studies. In particular, during (15 min after the end of the first emission scan) and after the PET scans, subjects were asked to void. The volume and radioactivity levels of their urine samples were measured using a calibrated well counter.

MRI study

All subjects underwent T1-weighted magnetic resonance imaging (MRI) scans using a Signa 1.5-T machine (General Electric Inc., Milwaukee, WI, USA) within a week of the PET scans. For each position (brain, chest, abdomen and epigastric region), individual T1-weighted scans with a voxel size of 1.875 × 1.875 × 6.000 mm (TR = 460 ms, TE = 14 ms, image matrix = 256 × 256 × 40) were obtained with subjects holding their breath.
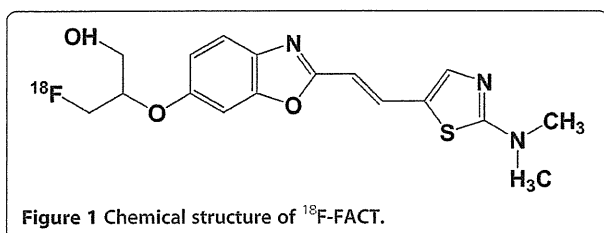
Dosimetry

The Medical Internal Radiation Dose committee of the Society of Nuclear Medicine developed the algorithm to calculate absorbed dose D (the energy deposited per unit mass of medium (Gy)) in organs. The basic idea is that radiation energy from the radioisotope in the source organ is absorbed in the target organs, and the algorithm requires the net accumulated radioactivity in source organs as an input [15]. A PET scan contributes to quantitative knowledge on the whole-body distribution of radioisotope. In the present study, the accumulated activity in source organs was derived from PET measurements and the organ volumes of the reference male or female. The mean absorbed dose to the kth target organ is defined as follows:

$$\bar{D}(r_k) = \sum_h \tilde{A}_h \times S(r_k \leftarrow r_h) = \sum_h A_0 \times \tau_h \times S(r_k \leftarrow r_h), \ \tau_h = \frac{\tilde{A}_h}{A_0}$$

(1)

where $S(r_k \leftarrow r_h)$ is the absorbed dose in the kth target organ per unit of accumulated activity in the hth source organ, called the S value. $\tilde{A}_h$ is the number of disintegrations in the hth source organ, A_0 is the injected dose, and τ_h is the time-integrated activity coefficient in the hth source organ (equal to the number of disintegrations per unit activity administered). The effective dose E (Sv), as defined by the International Commission on Radiological Protection (ICRP) 60 [10], was obtained using the following equation:

$$E = \sum_i Q \times w_i \times D_i$$

(2)

where D_i is the absorbed dose of the ith target organ, w_i is the weighting risk factor in the ith target organ, and Q is the quality factor ($Q = 1$ for β- and γ-rays).

Figure 1 Chemical structure of ^{18}F-FACT.

Figure 2 Overview of PET scan protocols. Four emission scans and two transmission scans (before and intermediate emission scans) with a $^{68}Ge/^{68}Ga$ source were performed. In particular, the second transmission scan was performed using a post-injection transmission scan.
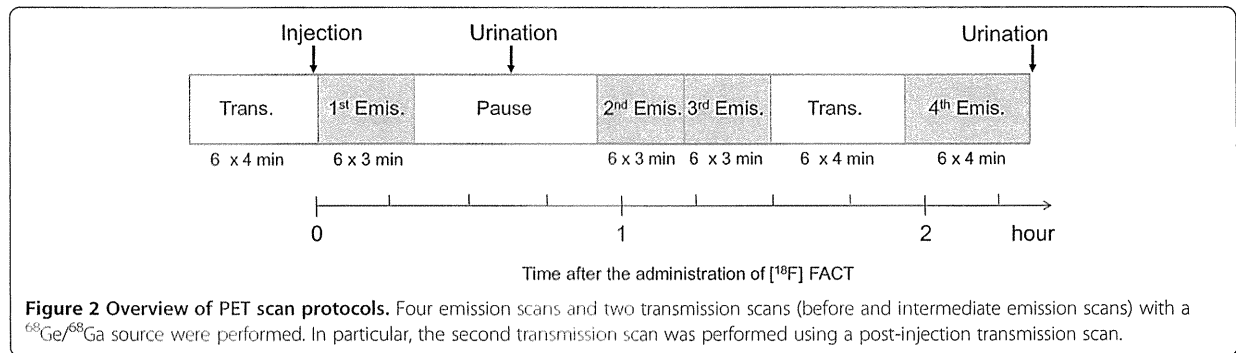
Regions of interest

The number of source organs used for region-of-interest (ROI) drawing was 19 for male and 20 for female subjects. A detailed list of source organs is shown in Table 2. Two nuclear medicine physicians manually drew the ROIs using PMOD version 3.1 (PMOD Technologies, Zurich, Switzerland). All individual PET images and MRI images were co-registered to the first individual PET images using a rigid matching module of the same PMOD with a dissimilarity function of normalised mutual information (for MRI-to-PET cases) and the sum of the absolute difference (for PET-to-PET cases) algorithms.

For visceral organs with extremely high uptake (liver and gallbladder), individual ROIs were defined at a fixed

Table 2 [^{18}F]FACT time-integrated activity coefficients in the source organs

Organ	Human (MBq-h/MBq)							Mouse (MBq-h/MBq)
	Mean ± 1 SD	Subject 1	Subject 2	Subject 3	Subject 4	Subject 5	Subject 6	
Adrenal gland	5.38E−04 ± 2.98E−04	9.40E−04	8.40E−04	5.20E−04	3.70E−04	4.00E−04	1.60E−04	-
Brain	4.20E−02 ± 8.44E−03	5.41E−02	3.68E−02	3.53E−02	4.87E−02	4.42E−02	3.26E−02	6.99E−03
Breast	8.40E−03 ± 4.37E−03	1.14E−03	8.25E−03	5.59E−03	1.16E−02	1.19E−02	1.19E−02	-
Gallbladder content[a]	2.22E−01 ± 1.05E−01	-	1.49E−01	2.27E−01	3.88E−01	1.16E−01	2.31E−01	-
Lower large intestine content	2.12E−02 ± 2.03E−02	5.91E−02	1.06E−02	4.80E−03	2.27E−02	2.40E−02	5.96E−03	-
Small intestine content	8.78E−02 ± 1.08E−01	7.40E−02	3.74E−02	3.34E−02	3.06E−01	3.36E−02	4.25E−02	1.22E−01
Stomach content	6.71E−03 ± 2.28E−03	5.22E−03	6.23E−03	9.29E−03	9.84E−03	4.78E−03	4.87E−03	-
Upper large intestine content	2.55E−02 ± 1.89E−02	1.48E−02	4.88E−02	1.01E−02	4.99E−02	2.04E−02	8.85E−03	-
Heart content	1.12E−02 ± 1.51E−03	1.24E−02	1.13E−02	1.02E−02	1.30E−02	1.15E−02	8.83E−03	3.95E−03
Heart wall	7.50E−03 ± 1.84E−03	4.63E−03	1.00E−02	8.84E−03	6.75E−03	7.28E−03	7.49E−03	2.39E−03
Kidney	1.34E−02 ± 3.27E−03	1.32E−02	1.16E−02	1.53E−02	1.89E−02	9.59E−03	1.20E−02	9.34E−03
Liver	4.92E−01 ± 1.05E−01	6.28E−01	5.85E−01	4.34E−01	5.15E−01	3.42E−01	4.49E−01	1.69E−01
Lung	3.55E−02 ± 1.16E−02	3.78E−02	5.31E−02	4.36E−02	2.46E−02	2.33E−02	3.08E−02	1.17E−02
Muscle	4.66E−01 ± 3.73E−01	9.43E−01	5.47E−01	7.97E−01	5.40E−02	4.12E−01	4.34E−02	1.57E−01
Ovary[b]	5.53E−04 ± 3.79E−05	-	-	-	5.70E−04	5.10E−04	5.80E−04	-
Pancreas	4.13E−03 ± 9.75E−04	6.10E−03	3.62E−03	3.93E−03	3.81E−03	3.55E−03	3.76E−03	-
Red marrow	3.98E−02 ± 4.33E−03	4.02E−02	3.83E−02	3.79E−02	4.59E−02	4.29E−02	3.34E−02	1.61E−02
Spleen	5.41E−03 ± 1.74E−03	8.64E−03	4.88E−03	3.83E−03	6.01E−03	4.77E−03	4.30E−03	1.28E−03
Testis[c]	5.77E−04 ± 4.67E−04	7.00E−04	6.10E−05	9.70E−04	-	-	-	-
Thyroid	3.53E−04 ± 1.55E−04	6.30E−04	3.70E−04	3.60E−04	2.40E−04	1.80E−04	3.40E−04	-
Urinary bladder contents	2.26E−02 ± 8.36E−03	1.70E−02	2.69E−02	1.55E−02	3.63E−02	2.49E−02	1.51E−02	6.56E−02
Uterus/uterine wall[b]	4.46E−03 ± 1.90E−03	-	-	-	6.42E−03	2.63E−03	4.33E−03	-
Remainder of the body	1.17 ± 3.63E−01	7.24E−01	1.06	9.48E−01	1.08	1.51	1.69	2.08

Averaged time-integrated activity coefficient (MBq-h/MBq) for the source organs (n = 6) from the whole-body PET data (n = 6) from experiments involving human subjects of [^{18}F]FACT and mice of [^{18}F]FACT. [a]Averaged value among five subjects excluding subject no. 1. [b]Average time-integrated activity coefficient among female subjects (n = 3). [c]Average time-integrated activity coefficient among male subjects (n = 3).

emission scan with about a 40% threshold against the maximum counts (first emission for the liver and third or fourth emission for the gallbladder). Then the ROI was applied to the other emission images with minor adjustment of its location or shape. For the intestines, if specific high uptake was observed, individual ROIs were defined on each time frame of the PET images with about a 10% threshold. If there was no specific high uptake in the intestines, and uptake could be regarded as uniform, individual ROIs were drawn around the corresponding area.

In order to obtain a typical radioactivity concentration within organs with less location mismatch between PET and the co-registered MRI images (brain, breast, heart wall, heart contents, kidney, liver, lung, muscle, bones, spleen and thyroid), individual ROIs were drawn on co-registered MRI images. For other low-uptake organs (adrenal gland, stomach contents, pancreas, ovary, uterus and testis), individual ROIs were drawn on each time frame of the PET images and referred to the co-registered MRI images. To avoid a partial volume effect, the size of the ROI for these MRI available organs was made slightly smaller than the entire source organ. It should also be noted that all activities in vertebrae ROIs was assumed to be in the red marrow in the present study.

Data analysis

Averaged time-activity curves for each organ were obtained using the ROI values from each subject's PET images. Because the PET images were decay-corrected at the start of each scan during the reconstruction procedure, the non-decay-corrected time-activity curves ($C(t)$, Bq/ml) were re-calculated. During each whole-body emission scan, the bed position was moved from the foot to the head (six bed positions in total). However, we assumed that PET counts at all bed positions were acquired at the mid-scan time. Then, individual radioactivity concentration per injected dose A_0 (Bq) was extrapolated into the percent injected dose (%ID) of the reference subject as follows:

$$\%ID(t)_{reference} = \left(\frac{C(t)}{A_0} \right)_{individual} \times V_{reference} \qquad (3)$$

where V (ml) is the organ volume, and $V_{reference}$ is V of the reference subject (we used a 70-kg adult male and 58-kg adult female as the male and female reference subjects) [16,17]. Even though some organs such as the intestine may change their volume over time, we used the reference subjects' organ volumes over the time period of the calculation of the %ID.

The time-integrated activity coefficient τ (Bq-h/Bq) in Equation 1 was obtained by fitting (%ID(t)) using a mono-exponential function and integrating from time zero to infinity. If the time-activity curve did not converge at the last PET scan (e.g. intestines and gallbladder), time-activity curves were fitted using two exponential functions, and then the area under the curve after the acquisition of the last image was calculated by assuming only physical decay of ^{18}F and no additional biologic clearance to be conservative [10]. The time-integrated activity coefficient for urinary bladder content was calculated by applying the dynamic urinary bladder model [10] to the urine samples with a bladder voiding interval of 2 h. The decay-corrected cumulative activity for urine was fitted using the equation $A \times (1 - \exp(-\ln (2) \times t / \tau))$, where τ is the biological decay and A is the fraction of activity released from the body. The sum of the time-integrated activity coefficient for the specific organs was subtracted from the time-integrated activity coefficient for the total body, which was calculated from the time integral of the decaying injected radioactivity. Then the residual of the subtraction was regarded as the time-integrated activity coefficient in the remainder of the body. All fitting procedures were undertaken using a mean fit of R^2 of 0.93 ± 0.13.

Finally, the time-integrated activity coefficient τ (Bq-h/Bq) was used to calculate the absorbed dose, D, in Equation 1 and the effective dose, E, in Equation 2. Both kinetics calculations (fitting and integration) and dose estimation were performed using OLINDA/EXM software version 1.0 (Department of Radiology and Radiological Sciences Vanderbilt University, Nashville, TN, USA) [17].

Animal experiments

The experimental protocols were reviewed by the Committee on the Ethics of Animal Experiments at Tohoku University School of Medicine and performed in accordance with the Guidelines for Animal Experiments issued by the Tohoku University School of Medicine. Estimated radiation dose of [18F]FACT in the human subjects calculated from mouse data sets was compared with those of [18F]FACT from human whole-body PET scans. An average dose of 1.4 MBq of [18F]FACT was intravenously injected into ICR mice (age, 6 weeks; average body weight, 30 g) without anaesthesia. In the [18F]FACT study, the mice were killed by cervical luxation at 2, 10, 30, 60 and 120 min ([18F]FACT) after administration (n = 4 at each time point). The masses of the blood, heart, lung, liver, spleen, small intestine, kidney, brain and urine samples were measured, and activity was also measured using a well counter. Thigh bone and muscle were also sampled. The average uptake of the

radioligand into the male reference subject (70 kg) was extrapolated as follows [18]:

$$\%ID(t)_{human} = \left(\frac{\%ID(t)}{mass_{organ}}\right)_{mouse} \times (mass_{body})_{mouse} \times \left(\frac{mass_{organ}}{mass_{body}}\right)_{human}$$

(4)

where the bodyweight of the mouse was assumed to be 30 for [^{18}F]FACT.

Finally, in the same manner as in the human PET data analysis, time-integrated activity coefficients, absorbed doses and effective doses were calculated using the OLINDA/EXM software version 1.0. Sampled blood, thighbone and urine were regarded as heart contents, red bone marrow and urinary bladder contents, respectively.

Results and discussion
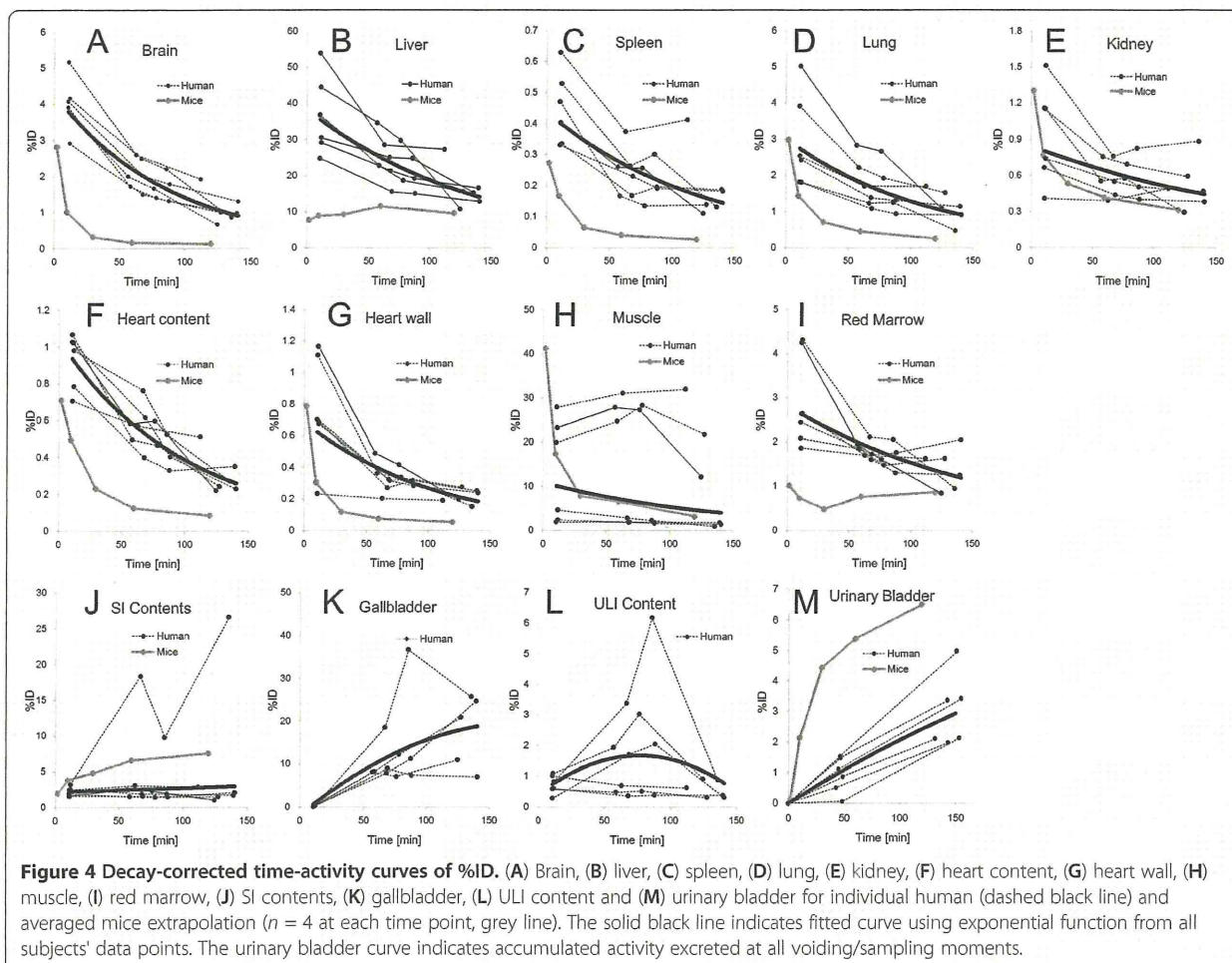### Biodistribution of [^{18}F]FACT
Figure 3A is the coronal PET image for a single female subject (no. 5) and demonstrates the typical biodistribution of [^{18}F]FACT in the human body. The highest accumulations of this radioligand were observed in the gallbladder, liver, intestine and urinary bladder. For subject no. 1, [^{18}F]FACT contained in the bile was excreted from the liver to the duodenum through the biliary tract (Figure 3B). The biodistribution pattern of [^{18}F]FACT in human subjects showed a predominant hepatobiliary excretion, which is similar to what has been observed for other amyloid ligands, such as [^{11}C] PIB, [^{18}F]AV-45, [^{18}F]GE067 and [^{18}F]BAY94-9172 [7,8,10,11].

Figure 4 shows the decay-corrected time-activity curve of the %ID for typical source organs (brain, liver, spleen, lung, kidney, heart content, heart wall, muscle, red marrow, small intestine contents, gallbladder, upper large intestine contents and urinary bladder) from the six volunteers and the mice experiments. A significant difference between the %ID from humans and mice was observed in the brain, liver, spleen, heart contents, red marrow and urinary bladder, and these differences propagated the different results regarding dose estimation. In human subjects, ^{18}F uptake in the gallbladder contents and the intestines (Figure 4J,K,L) indicated larger individual variations in radioactivity uptake relative to other organs (e.g. the kidney as shown in Figure 4E). Radioactivity uptake in the upper large intestine showed propagation of both ligand kinetics and inter-subject variation from the gallbladder (Figure 4K,L). Scheinin et al. previously reported that inter-subject variation in ligand uptake ([^{11}C]PIB) in the gallbladder may be due to the quality and quantity of post-injection food intake [7]. In the present study, the subjects drank water during the interval between the first and second PET scans. This may have been responsible for the increase in inter-subject variation regarding the gallbladder. Furthermore, because the gallbladder uptake in some subjects had declined or remained at a low level at the final time points, we assumed that there was only physical radioactive decay after the last PET scans. However, this assumption may have led to a conservative estimation of the absorbed dose.

Figure 5 presents typical brain PET images obtained using [^{18}F]FACT at different time points with an
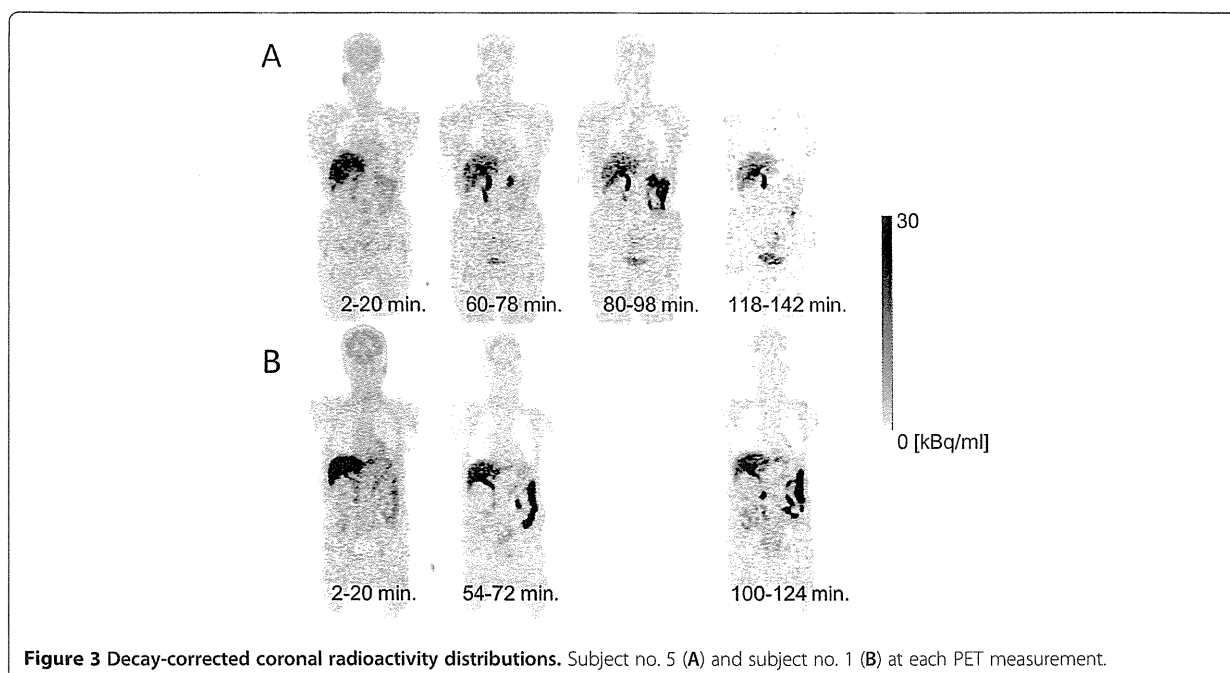
Figure 3 Decay-corrected coronal radioactivity distributions. Subject no. 5 (**A**) and subject no. 1 (**B**) at each PET measurement.

Figure 4 Decay-corrected time-activity curves of %ID. (A) Brain, **(B)** liver, **(C)** spleen, **(D)** lung, **(E)** kidney, **(F)** heart content, **(G)** heart wall, **(H)** muscle, **(I)** red marrow, **(J)** SI contents, **(K)** gallbladder, **(L)** ULI content and **(M)** urinary bladder for individual human (dashed black line) and averaged mice extrapolation ($n = 4$ at each time point, grey line). The solid black line indicates fitted curve using exponential function from all subjects' data points. The urinary bladder curve indicates accumulated activity excreted at all voiding/sampling moments.

acquisition time of 3 min (first, second and third emission) and 4 min (fourth emission). There was no significant retention of [^{18}F]FACT in the brain, and this may have been because the subject was normal.

Estimated dose of [^{18}F]FACT

The [^{18}F]FACT time-integrated activity coefficients in the source organs are shown in Table 2, and the absorbed doses are shown in Table 3. The averaged time-integrated activity coefficient for the gallbladder, as shown in Table 2, was calculated among five subjects

excluding subject no. 1; however, in the case of the averaged absorbed and effective doses, subject no. 1 was included (Table 3).

High absorbed dose in humans was observed in the gallbladder (333 ± 251 μGy/MBq), liver (77.5 ± 14.5 μGy/MBq), small intestine (33.6 ± 30.7 μGy/MBq), upper large intestine (29.8 ± 15.0 μGy/MBq) and lower large intestine (25.2 ± 12.6 μGy/MBq). In mice, high absorbed doses were observed in the small intestine (38.5 μGy/MBq), liver (25.5 μGy/MBq) and urinary bladder wall (43.1 μGy/MBq) for [^{18}F]FACT (Table 3).
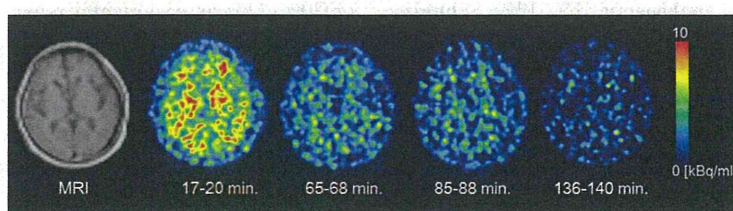
Figure 5 Decay-corrected brain PET images of subject no. 3 at different time points.

Table 3 Absorbed doses in the source organs

	Human			Mouse
	All subjects (*n* = 6)	Male (*n* = 3)	Female (*n* = 3)	
Organ				
Adrenal gland	1.96E01 ± 2.00	2.03E01	1.90E01	1.35E01
Brain	9.91 ± 1.82	8.95	1.09E01	4.17
Breasts	8.69 ± 2.55	6.68	1.07E01	9.90
Gallbladder wall	3.33E02 ± 2.51E02	2.16E02	4.50E02	1.68E01
Lower large intestine wall	2.52E01 ± 1.26E01	2.41E01	2.63E01	1.57E01
Small intestine	3.36E01 ± 3.07E01	2.07E01	4.64.E01	3.85E01
Stomach wall	1.61E01 ± 3.44	1.35E01	1.87E01	1.39E01
Upper large intestine wall	2.98E01 ± 1.50E01	2.36E01	3.59E01	1.83E01
Heart wall	1.62E01 ± 1.70	1.50E01	1.74E01	8.34
Kidneys	2.01E01 ± 4.30	1.85E01	2.17E01	1.32E01
Liver	7.75E01 ± 1.45E01	7.38E01	8.11E01	2.55E01
Lungs	1.46E01 ± 1.10	1.49E01	1.43E01	7.96
Muscle	1.03E01 ± 1.27	1.07E01	9.90	7.89
Ovary	1.67E01 ± 6.65	1.18E01	2.16E01	1.67E01
Pancreas	2.32E01 ± 3.11	2.17E01	2.47E01	1.45E01
Red marrow	1.31E01 ± 1.70	1.16E01	1.46E01	1.23E01
Osteogenic cells	1.60E01 ± 3.65	1.25E01	1.95E01	1.82E01
Skin	7.30 ± 1.39	5.99	8.60	8.70
Spleen	1.37E01 ± 2.48	1.27E01	1.48E01	7.83
Testis	7.32 ± 2.16	7.32	-	1.15E01
Thymus	1.00E01 ± 1.85	8.37	1.16E01	1.08E01
Thyroid	8.36 ± 1.38	8.86	7.86	1.10E01
Urinary bladder wall	2.23E01 ± 7.33	1.81E01	2.66E01	4.31E01
Uterus	1.67E01 ± 8.13	1.14E01	2.19E01	1.77E01
Total body	1.38E01 ± 1.63	1.22E01	1.53E01	1.22E01
Effective dose (µSv/MBq)	1.86E01 ± 3.74	1.64E01	2.09E01	1.48E01

Averaged absorbed dose estimates (µGy/MBq) for the target organs from the whole-body PET data (*n* = 6) from experiments involving human subjects of [18F] FACT and mice of [18F]FACT. Average absorbed dose for male subjects (*n* = 3).

The effective dose estimated from the human PET study was 18.6 ± 3.74 µSv/MBq. The effective doses of [18F]FACT estimated from the clinical PET studies among other [18F]-labelled PET amyloid radioligands were as follows: [18F]AV-45, 13 and 19.3 µSv/MBq [8,9]; [18F] GE067, 33.8 µSv/MBq [10]; and [18F]BAY94-9172, 14.67 µSv/MBq [11]. For PET analysis of [11C]PIB, Scheinin et al. normalised the %ID using the ratio of individual and reference subjects' body weights (Equation 4) [7]. However, in the present study, we did not normalise the %ID data because there was a small difference between the effective dose with normalisation (17.6 ± 2.12 µSv/MBq) and the present effective dose (18.6 ± 3.74 µSv/MBq). Therefore, we concluded that body weight normalisation does not influence the effective dose.

The effective dose of [18F]FACT from the mouse experiments (14.8 µSv/MBq) was underestimated as compared with that from the human subject PET studies (18.6 µSv/MBq) (Table 3). This discrepancy corresponded to 0.76 mSv (2.96 and 3.72 mSv from mice and humans, respectively) while assuming an injected activity of 200 MBq as a clinically relevant dose. The underestimation of absorbed dose in the mouse gallbladder (20 times lower) and liver (3 times lower) relative to the human PET studies may have been responsible for the underestimation of the effective dose. High absorbed doses in the liver, gallbladder and small intestine of mice indicated that the biodistribution pattern of [18F]FACT in mice includes hepatobiliary excretion, as was observed in the PET scans involving human subjects. However,